Charge radii of neon isotopes across the *sd* neutron shell

K. Marinova,[1,2] W. Geithner,[1] M. Kowalska,[3] K. Blaum,[4] S. Kappertz,[1] M. Keim,[3] S. Kloos,[1] G. Kotrotsios,[1] P. Lievens,[5] R. Neugart,[1] H. Simon,[6] and S. Wilbert[1]

[1]*Institut für Physik, Universität Mainz, D-55099 Mainz, Germany*
[2]*Laboratory of Nuclear Reactions, Joint Institute of Nuclear Research, 141980 Dubna, Russia*
[3]*Physics Department, CERN, CH-1211 Geneva 23, Switzerland*
[4]*Max-Planck-Institut für Kernphysik, D-69117 Heidelberg, Germany*
[5]*Laboratorium voor Vaste-Stoffysica en Magnetisme, K.U.Leuven, B-3001 Leuven, Belgium*
[6]*Institut für Kernphysik, TU Darmstadt, D-64289 Darmstadt, Germany*

(Received 29 April 2011; published 12 September 2011)

We report on the changes in mean square charge radii of unstable neon nuclei relative to the stable ^{20}Ne, based on the measurement of optical isotope shifts. The studies were carried out using collinear laser spectroscopy on a fast beam of neutral neon atoms. High sensitivity on short-lived isotopes was achieved thanks to nonoptical detection based on optical pumping and state-selective collisional ionization, which was complemented by an accurate determination of the beam kinetic energy. The new results provide information on the structural changes in the sequence of neon isotopes all across the neutron *sd* shell, ranging from the proton drip line nucleus and halo candidate ^{17}Ne up to the neutron-rich ^{28}Ne in the vicinity of the "island of inversion." Within this range the charge radius is smallest for ^{24}Ne with $N = 14$ corresponding to the closure of the neutron $d_{5/2}$ shell, while it increases toward both neutron shell closures, $N = 8$ and $N = 20$. The general trend of the charge radii correlates well with the deformation effects which are known to be large for several neon isotopes. In the neutron-deficient isotopes, structural changes arise from the onset of proton-halo formation for ^{17}Ne, shell closure in ^{18}Ne, and clustering effects in ^{20,21}Ne. On the neutron-rich side the transition to the island of inversion plays an important role, with the radii in the upper part of the *sd* shell confirming the weakening of the $N = 20$ magic number. The results add new information to the radii systematics of light nuclei where data are scarce because of the small contribution of nuclear-size effects to the isotope shifts which are dominated by the finite-mass effect.

DOI: 10.1103/PhysRevC.84.034313 PACS number(s): 21.10.Ft, 27.20.+n, 27.30.+t, 31.30.Gs

I. INTRODUCTION

Studies of light unstable nuclei have revealed many interesting phenomena absent or little visible in heavier systems [1]. To these belong unexpected nucleon density distributions such as the well-established neutron halos and skins, hints (or predictions) of proton halos, and clusterlike structures. In addition, changes were observed in magic numbers, which have been the cornerstone of the nuclear shell model for half a century.

The Ne, Na, and Mg isotopic chains, with $Z = 10$–12 and spanning the neutron *sd* shell and beyond, have provided us with examples or candidates of all above phenomena. Proton-rich ^{17}Ne is a candidate for a two-proton halo [2,3], cluster structures have been found in $^{20-22}$Ne and ^{24}Mg [4], and the isotopes around $N = 20$ make up the so-called island of inversion [5], where a weakening or even disappearance of the neutron magic number is visible.

The purpose of this paper is to extend our knowledge of the nuclei in this region by investigating the charge radii of neutron-rich neon isotopes based on their optical isotope shifts compared to stable ^{20}Ne. Until now sodium was the only element for which isotope shift measurements cover the neutron *sd* shell between the $N = 8$ and 20 shell closures. However, the presence of only one stable isotope in this chain set a serious constraint on the accuracy of the radii differences extracted from isotope shifts [6,7]. On the other hand, neon, with three stable isotopes, is the first element for which accurate radii can be obtained from the proton drip line at $N = 7$ (^{17}Ne) over most of the *sd* shell, up to $N = 18$ (^{28}Ne). The neutron drip line of neon ($N = 22$) is very close to the magic number $N = 20$ and therefore the study of these isotopes is a good testing ground to examine both the systematics of deformation and the possible erosion of the $N = 20$ spherical shell closure in the vicinity of the neutron drip line. These phenomena allude to the persistence of shell gaps and magic numbers away from the valley of stability.

The reported hyperfine structures and isotopes shifts of radioactive Ne isotopes with $A = 17$–$26, 28$ have been measured by collinear fast-beam laser spectroscopy, which provides information on the changes of nuclear mean square charge radii $\delta\langle r^2\rangle$, nuclear spins, and electromagnetic moments μ and Q. In our previous work [8] the magnetic dipole moments of ^{17}Ne, ^{23}Ne, and ^{25}Ne, as well as the electric quadrupole moment of ^{23}Ne, were either reported for the first time or improved considerably. These measurements also decided for a $1/2^+$ ground state of ^{25}Ne. Recently, we have also reported on the charge radii of neutron-deficient isotopes $^{17-22}$Ne together with high-precision data on their masses [9], the latter obtained by Penning trap mass spectrometry. Microscopic calculations within the fermionic molecular dynamics (FMD) approach describe remarkably well the behavior of the charge radii and binding energies, and can explain them by pronounced changes in the structure of the nuclear ground states.

Isotope shift measurements using laser spectroscopy techniques meet serious limitations for light elements with proton

number below $Z = 20$. This is because of the fact that the field shift contribution, considered to be proportional to $\delta\langle r^2\rangle$, becomes very small relative to the total isotope shift which is dominated by a second part, namely the finite-mass shift. Thus, systematic effects which do not disturb studies on heavier nuclei have to be well under control. In particular, collinear laser spectroscopy on a fast beam involves large Doppler shifts of which the uncertainty, arising from voltage measurements, can mask the field shift effects. The requirement of high experimental accuracy and knowledge of the mass shift scaling constant then adds to the standard sensitivity problem faced by experiments on weak beams of short-lived isotopes. In the reported studies the accuracy requirement was met by an accurate determination of the beam kinetic energy [10] utilizing a novel method of comparing Doppler-shifted transition frequencies. At the same time, the high sensitivity and selectivity were achieved using ultrasensitive nonoptical detection based on optical pumping, state-selective collisional ionization, and observation of the β decay of collected radioactive ions [11,12].

The experimental setup and the methods used to achieve the accuracy of measurements are discussed in Sec. II. The experimental results are presented in Sec. III, while the measured nuclear radii are discussed and compared to other data and to nuclear models in Sec. IV.

II. EXPERIMENT

A. Experimental setup

The experiment was performed at the ISOLDE on-line isotope separator using a 1.4-GeV pulsed beam of about 3×10^{13} protons every 2.4 s from the CERN PS-Booster synchrotron. Radioactive neutron-deficient neon isotopes were produced by spallation reactions in a CaO target, while neutron-rich isotopes were obtained from fragmentation of uranium in a UC_2 target (see Table I). Together with stable isotopes of a neon-xenon gas mixture these are ionized in a plasma source, accelerated to 60 keV and mass selected by the ISOLDE GPS separator [13].

TABLE I. Half-lives $T_{1/2}$ of the investigated Ne isotopes; targets used for production and yields.

A	$T_{1/2}$	Target	Yield per pulse (or current)
17	109.2 ms	CaO	3.6×10^3
18	1.67 s	CaO	2.5×10^5
19	17.34 s	CaO	2.0×10^6
20	stable	–	<40 nA
21	stable	–	<4 nA
22	stable	–	<100 pA
23	37.24 s	CaO/UC_2	3×10^6
24	3.38 min	UC_2	3.5×10^5
25	602 ms	UC_2	7×10^4
26	197 ms	UC_2	3.2×10^4
27	32 ms	UC_2	<200
28	17 ms	UC_2	<70

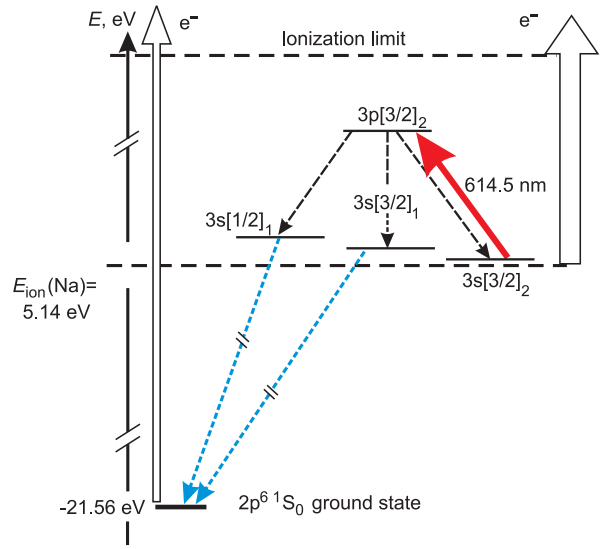

FIG. 1. (Color online) Partial atomic level scheme [15] of neon including transitions involved in the charge-exchange neutralization, optical pumping, and collisional ionization.

The isotope shifts and hyperfine structures of the investigated isotopes were measured in the transition $2p^5 3s[3/2]_2 \rightarrow 2p^5 3p[3/2]_2$ ($\lambda = 614.5$ nm) of the atomic spectrum of neon, using the technique of collinear fast-beam laser spectroscopy combined with ion detection of optical resonance [14]. The mass-separated ion beam is superimposed collinearly on a cw dye laser beam. The ions are then neutralized by charge exchange in a sodium vapor cell. The charge-exchange reaction populates predominantly the metastable $2p^5 3s[3/2]_2$ state, because its binding energy matches well the ionization energy of the sodium atom. A sodium vapor pressure of the order of 10^{-2} mbar, at a temperature of about 550 K, was sufficient to achieve charge-exchange efficiencies up to 90%. Atoms in the metastable state are excited resonantly by laser light to the $2p^5 3p[3/2]_2$ level which decays either back to $2p^5 3s[3/2]_2$ or cascades with high probability via the intermediate $2p^5 3s[1/2, 3/2]_1$ states to the $2p^6\,{}^1S_0$ ground state (see Fig. 1).

The experimental apparatus, procedure, and detection technique have already been described in our previous papers [8,12,16] (see Fig. 2). The nonoptical detection of atomic resonance is based on collisional ionization [14] for which different cross sections discriminate between the population of the metastable state and the ground state. At resonance, optical pumping occurs from the metastable state to the ground state and thus gives rise to a decrease in the ionization rate. The ions are deflected out of the original beam direction and counted with the help of a secondary electron multiplier. For short-lived isotopes it is more favorable to detect the radioactive β decay of the collected ions, because it is insensitive to background from isobaric (stable) beam contamination. To eliminate fluctuations of the ion signal caused by intensity fluctuations of the primary ion beam, we have introduced a normalization procedure as described below. Reasons for these fluctuations are variations of the proton-beam intensity and changing target heating conditions from an irregular proton

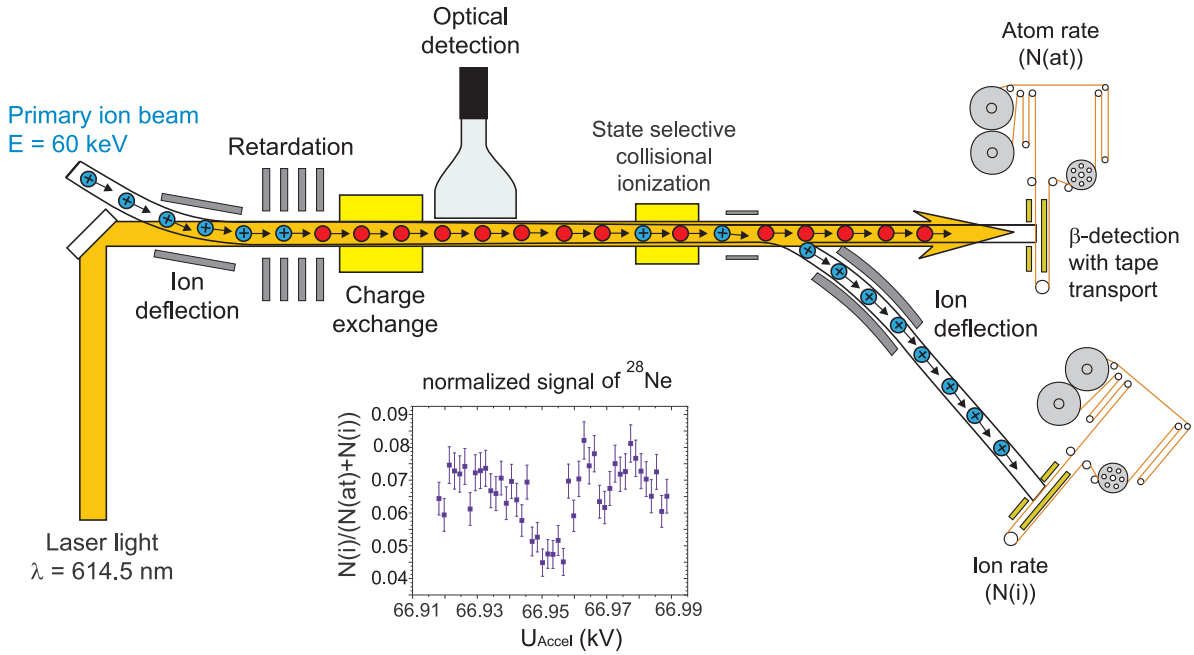

FIG. 2. (Color online) Schematic view of the experimental setup with fluorescence and alternative ion- and β-detection schemes. The inset shows a normalized experimental spectrum for ^{28}Ne, which was obtained using β detection and summation of individual scans (each of duration of about 1.5 min) over 4.5 h.

pulse time structure caused by the distribution of pulses to different accelerators and experiments at CERN.

The selective ionization of metastable atoms occurs in the passage of the beam through a thin Cl_2 gas target. The ions are then deflected onto a tape surrounded by scintillators for β-radioactivity counting. Every collected sample corresponds to the activity produced by one proton pulse, and the tape is moved after counting, thus carrying away long-lived daughter activity or background, before another sample is taken for the next data point.

The problem of normalization was overcome by installing another detector system in the forward direction, identical to the one in the deflected direction (see Fig. 2). Thus, the count rate from the neutral fraction of the beam was recorded in parallel. Normalizing the ion signal to the total beam intensity gives a signal which is independent of beam intensity fluctuations:

$$S = \frac{N(\text{ion})}{N(\text{ion}) + N(\text{atom})}. \tag{1}$$

Here S is the normalized signal, N(ion) and N(atom) are the corresponding count rates of ions and neutral atoms. The sensitivity of this scheme is demonstrated in the inset of Fig. 2, where a resonance curve for ^{28}Ne with a half-life of 17 ms and a yield of about 45 ions per pulse from ISOLDE is shown.

Spectra of longer-lived isotopes taken by direct ion counting were recorded in a fast repeated scanning mode, thus averaging over all systematic variations and statistical fluctuations of the beam intensity. As for some of the isotopes the measuring times added up to a few hours, we used a long-term laser frequency stabilization based on a frequency-stabilized HeNe laser in addition to the standard active frequency stabilization (Coherent 699-21 system).

B. Voltage calibration

Most conveniently for collinear laser spectroscopy measurements the laser frequency ν_L is kept constant. Tuning the excitation frequency is then achieved by changing the atom beam velocity, with the neutralization region at a variable electrical potential. The position of an atomic resonance is determined by the total kinetic energy of the atoms (about 60 ± 10 keV) at resonance with the optical transition. The Doppler-shifted frequency is related to the resonance frequency ν_0 of the atomic transition in the rest frame of the atoms:

$$\nu(\beta) = \nu_L = \nu_0 \frac{1 \pm \beta}{\sqrt{(1-\beta^2)}}, \text{ with } \beta = \frac{\sqrt{eU(eU + 2mc^2)}}{eU + mc^2}. \tag{2}$$

Here the $+$ $(-)$ sign denotes the Doppler shift for atomic and laser beams propagating in the same (opposite) direction. The relative beam velocity $\beta = v/c$ is given by the relativistic expression in terms of the beam energy eU and isotope mass m. According to Eq. (2), the difference in Doppler shift between two neighboring neon isotopes is of the order of 30 GHz. The expected nuclear volume shift is about 10 MHz or smaller. Measuring this very small effect of 3×10^{-4} requires an accuracy better than 3×10^{-5} for the atom kinetic energy (i.e., less than 2 eV on 60 keV).

The actual beam energy is determined by the total electrical potential difference experienced by the ions:

$$U_{\text{tot}} = U_{\text{beam}} - U_{\text{post}} = U_{\text{acc}} + U_{\text{ion}} - U_{\text{post}}\,, \tag{3}$$

where U_{acc} is the ISOLDE acceleration voltage which determines largely the initial velocity of the mass-separated ion beam. U_{post} is the postacceleration voltage applied to the charge-exchange cell for tuning the atoms into resonance by the Doppler effect. Both, U_{acc} being typically 60 keV and U_{post} being in the range of -10 kV to $+10$ kV, are routinely measured by precision voltage dividers with absolute accuracies of 10^{-4}. This already turns out to be insufficient for the measurement of field isotope shifts in an element as light as neon.

However, the beam energy from ISOLDE is not only determined by the applied acceleration voltage, but also by the plasma potential U_{ion} at which the ions are created in the ion source. To ionize noble gases, the plasma source is operated at typically 130 V, however the ionization takes place in a volume inside the source of which the potential is not accessible to a direct measurement.[1] Therefore, without any better knowledge about the beam energy, the poorly known plasma potential U_{ion} would be the most important accuracy limitation for isotope shift measurements.

1. Beam energy measurement by collinear laser spectroscopy

We have used a convenient method of directly measuring the beam kinetic energy [10], which is offered by the atomic spectrum of neon. This is a modification of the technique described by Poulsen [17] and is based on the fact that two optical transitions, separated by twice the Doppler shift, can be excited with the same laser frequency applied in collinear and anticollinear laser beam versus atom beam geometry. This frequency can be expressed by the condition

$$\begin{aligned}\nu_L &= \frac{{\nu_0}^+}{mc^2}[mc^2 + eU^+ + \sqrt{eU^+(2mc^2 + eU^+)}] \\ &= \frac{{\nu_0}^-}{mc^2}[mc^2 + eU^- - \sqrt{eU^-(2mc^2 + eU^-)}],\end{aligned} \tag{4}$$

where ${\nu_0}^+$ and ${\nu_0}^-$ are the rest frame frequencies and U^+ and U^- are the acceleration voltages at resonance for collinear and anticollinear excitation, respectively. The resonance positions coincide at a beam energy $eU_c = eU^+ = eU^-$ which can be determined from Eq. (4):

$$eU_c = \frac{mc^2(\sqrt{{\nu_0}^+} - \sqrt{{\nu_0}^-})^2}{2\sqrt{{\nu_0}^+{\nu_0}^-}}. \tag{5}$$

The corresponding laser frequency according to (4) and (5) is given by

$$\nu_L = \sqrt{{\nu_0}^+{\nu_0}^-}. \tag{6}$$

[1]In earlier works on collinear laser spectroscopy with noble gases it was estimated, based on the voltage applied to the plasma ion source, to be close to the anode potential with an uncertainty of about 20–30 V [12].

Equation (5) can then be used to determine the energy of an ion beam at resonance with the laser, if the transition frequencies are known with sufficient accuracy.

2. Neon levels used in the experiment

Two transitions offered by the neon atomic spectrum can be used to calibrate beam energies of about 60 keV. Both of them start from the common $2p^5 3s[3/2]_2$ metastable state, populated in the charge-transfer reaction (see Fig. 3). Then the collinear excitation $2p^5 3s[3/2]_2 \rightarrow 2p^5 3p'[3/2]_1$ with ${\nu_0}^+ = 16730.2704470(87)$ cm^{-1} [18], and the anticollinear excitation $2p^5 3s[3/2]_2 \rightarrow 2p^5 3p'[3/2]_2$ with ${\nu_0}^- = 16816.666340(20)$ cm^{-1} [19] can be detected in the same way by collisional ionization and ion counting as described in Sec. II A. The quoted wave numbers for ^{20}Ne serve as a secondary wavelength standard and are very precisely known (to about 10^{-10}) from literature.

Calibration measurements were performed with the stable neon isotopes ^{20}Ne and ^{22}Ne. For ^{20}Ne, the beam energy corresponding to coinciding resonances according to Eq. (5) is $eU_c = 61758.77$ eV. This is well inside the working range used for collinear laser spectroscopy on the different isotopes. The Doppler-shifted transition frequency at this beam energy according to (6) becomes $\nu_L = 16773.4128$ cm^{-1}, corresponding to the easily accessible dye laser wavelength of $\lambda = 596.2$ nm.

For ^{22}Ne the corresponding wave numbers are obtained using known values of the isotope shifts in both lines: $\delta\nu^+ = 1728.79(16)$ MHz [18] and $\delta\nu^- = 1715.3(1.8)$ MHz which is the weighted mean value from [20–23]. In this case the resonances coincide at a beam energy of $eU_c = 67932.53$ eV.

3. Collinear-anticollinear measurements and results

To excite the atoms simultaneously in the collinear and in the anticollinear direction, a mirror was installed at the end window of the vacuum beam line. It reflects the laser

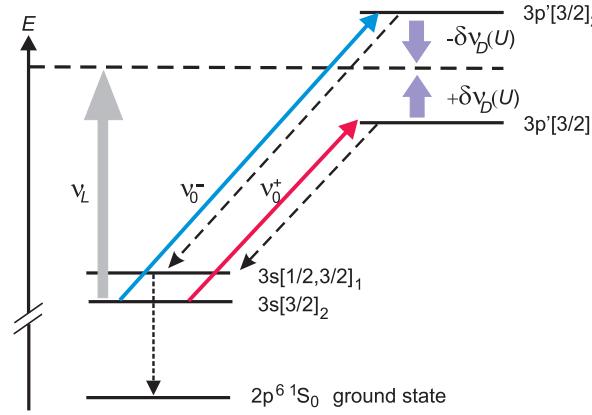

FIG. 3. (Color online) Partial atomic level scheme of neon [15] showing the transitions excited simultaneously with a collinear and anticollinear laser beam of the given laser frequency ν_L (thick full-line arrows). The dashed-line arrows indicate the radiative de-excitation to the ground state.

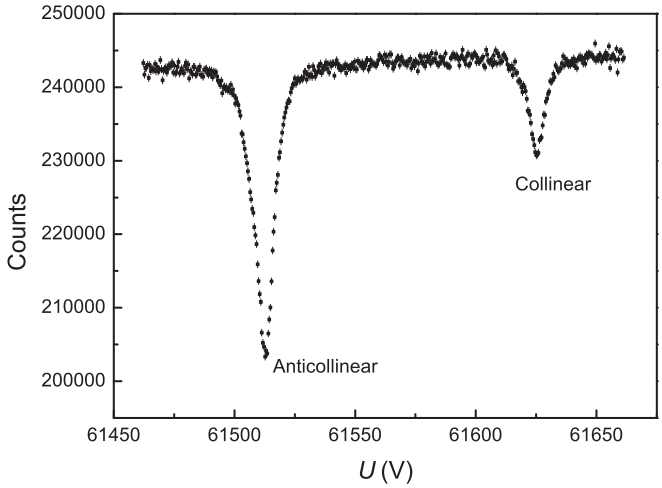

FIG. 4. Typical spectrum of ^{20}Ne with simultaneous collinear-anticollinear excitation.

beam back in itself. The excitation and detection of both the collinear and anticollinear resonances is performed in a narrow scan of the postacceleration voltage at fixed laser frequency. An example of a recorded spectrum for ^{20}Ne is shown in Fig. 4. The laser frequency is detuned from the value given by Eq. (6) by a few 100 MHz and both lines, originating from the collinear and anticollinear excitations, are well separated instead of overlapping. This facilitates the precise determination of the peak positions and the small correction according to their voltage difference has no influence on the accuracy of the beam energy measurement which is accurate to less than 1 eV.

Applying this procedure for both ^{20}Ne and ^{22}Ne, and using Eqs. (3) and (4) we are able to calibrate independently the effective acceleration voltage ($U_{\rm acc} + U_{\rm ion}$) and the scaling factor $D_{\rm div}$ involved in the measurement of the postacceleration voltage using a voltage divider. The uncertainties of ± 0.31 V on ($U_{\rm acc} + U_{\rm ion}$) and on $D_{\rm div} = 1000.00(3)$ are mainly systematic, arising from the uncertainty in the wave numbers of the transitions, the atomic masses of ^{20}Ne or ^{22}Ne expressed in eV, possible deviation from collinearity of the laser and atom beams and linearity of the tuning voltage. The ion sources used in different experimental runs are optimized for maximum yield. It turns out that for most sources this is equivalent to plasma conditions where the ions start from a potential surface very close (i.e., less than ± 5 V) to the anode potential.

C. Experimental procedure

Beam energy calibration measurements were performed at the beginning and at the end of each experimental run of typically three days. During the measurements on radioactive isotopes the acceleration voltage was monitored and the ion-source parameters were kept constant. Before and after each measurement on a radioactive isotope, resonances of two stable reference isotopes, ^{20}Ne and ^{22}Ne, were recorded using the fluorescence detection method which is suitable for much stronger beams. This was performed by switching simultaneously between different masses transmitted through the separator magnet and between preselected postacceleration voltages to which the scanning voltage was added for recording the spectra. These consist of single resonances for even-A isotopes or complete hyperfine structure patterns for odd-A isotopes. The frequency difference between the reference isotopes ^{20}Ne and ^{22}Ne as well as the absolute line positions provide an on-line test for the stability of the laser frequency and the high voltage.

All resonances of radioactive isotopes were detected nonoptically utilizing the collisional ionization method. Special care was taken to account for any artificial shifts between these and the reference lines observed in fluorescence. Such shifts could arise from different line shapes caused by different experimental conditions: Only atoms within the light collection region contribute to the fluorescence signal, whereas the ion signal is produced by optical pumping all along the beam from the charge-exchange cell to the ionizing gas target. In addition, low laser power is used with fluorescence detection to prevent optical pumping while high power is needed to produce maximum pumping and ionization efficiency with weak beams of unstable isotopes. Tests on the stable isotopes (^{20}Ne or ^{22}Ne) were performed by measuring the same resonance using both methods in parallel. As a result of numerous measurements at various conditions, a small systematic deviation was observed for the positions of the lines detected by ion counting ($U^{\rm ID}$) against those detected in fluorescence ($U^{\rm FD}$):

$$\delta U_{\rm corr} = U^{\rm FD} - U^{\rm ID} = -0.145(12)\,{\rm V}, \qquad (7)$$

corresponding to a frequency shift correction of about -1.5 MHz. All signals recorded with optical detection and low laser power were corrected by this voltage difference.

Centroids of all observed peaks were determined by fitting the lines with a convolution of a Lorentzian-shaped resonance and an exponential function. As shown and discussed before [24], this is a realistic model for the line shape, accounting for the partial energy loss in inelastic channels of the charge-transfer reaction by which the ion beam is neutralized. For any particular hyperfine structure or isotope shift measurement it is important to use common line-shape parameters of all resonances involved.

III. EXPERIMENTAL RESULTS

A. Isotope shifts

Isotope shifts in the transition $3s[3/2]_2 \rightarrow 3p[3/2]_2$ measured for $^{24-26,28}$Ne, together with already published data on $^{17-22}$Ne [9] are listed in Table II. The statistical errors of the isotope shifts arise from uncertainties of the resonance positions (even-A isotopes) or the positions of centers of gravity of the hyperfine structure (odd-A isotopes). They are mainly from counting statistics and contain a small digitizing error from the reading of the postacceleration voltage. The statistical errors are given in parentheses. The errors in square brackets are systematic errors. This error notation will be followed throughout the paper. For the isotope shifts $\delta\nu^{20,A}$ systematic errors arise mainly from the uncertainty of the acceleration voltages used to account for the Doppler shifts. The uncertainty of atomic masses [9,25] contributes less than 1 MHz, except for ^{28}Ne where it contributes 3.2 MHz.

TABLE II. Isotope shifts and changes in mean square charge radii of Ne isotopes. Errors in parentheses are statistical. Errors quoted in square brackets are systematic. For the isotope shifts $\delta\nu^{20,A}$ these are essentially from uncertainties of the acceleration voltages. The systematic errors of $\delta\langle r^2\rangle^{20,A}$ reflect the uncertainty of the field and mass shift constants (see text).

A	$\delta\nu^{20,A}$ (MHz)	$\delta\langle r^2\rangle^{20,A}$ (fm^2)
17	−3183.3(1.2)[3.3]	0.220(29)[123]
18	−1995.53(62)[2.09]	−0.207(15)[112]
19	−947.39(74)[99]	0.017(19)[41]
21	874.94(56)[90]	−0.217(14)[24]
22	1663.58(17)[1.72]	−0.321(4)[43]
23	2393.8(1.4)[2.5]	−0.571(34)[64]
24	3053.54(75)[3.16]	−0.627(19)[75]
25	3653.48(66)[3.79]	−0.429(16)[122]
26	4215.79(71)[4.37]	−0.484(18)[143]
28	5208.8(1.4)[5.4]	−0.239(35)[213]

The isotope shift between the stable ^{20}Ne and ^{22}Ne was already reported by several authors [20–23,26], the value of 1663.7(5.0) MHz given in [21] being closest to our data. The weighted mean value of $\delta\nu^{20,22}$ from all previous papers is 1662.3(1.7) MHz, which is also in agreement with the result of the present work.

B. Extraction of the mean square nuclear charge radii changes

The isotope shift can be decomposed into the field shift $\delta\nu_{\rm FS}^{20,A}$ and two terms accounting for the finite mass of the nucleus, the normal and specific mass shifts, $\delta\nu_n^{20,A}$ and $\delta\nu_s^{20,A}$ [27]:

$$\begin{aligned}\delta\nu^{20,A} &= \delta\nu_{\rm FS}^{20,A} + \delta\nu_n^{20,A} + \delta\nu_s^{20,A} \\ &= F\,\delta\langle r^2\rangle + (M_n + M_s)\frac{m_A - m_{20}}{m_A m_{20}}\,. \end{aligned} \tag{8}$$

Here, M_n and M_s are the normal and specific mass shift constants, and F is the electronic field shift factor. The latter can be calculated using a semiempirical approach based on the Goudsmit-Fermi-Segrè formula [27]. Following this procedure outlined in [28], we obtain for the investigated transition of neon:

$$F = -40[4]\,\text{MHz/fm}^2, \tag{9}$$

conventionally assuming an error of 10%. A similar value is obtained from an analysis of the hyperfine structure in the $2p^5 3s[3/2]_2$ metastable state.

The normal mass shift constant is $M_n = \nu m_e = 267.6$ GHz u, where m_e is the electron mass. The specific mass shift constant M_s takes into account correlations of the electron motion. Theoretical calculations of specific mass shifts are very difficult and the results available for a few cases reproduce the experimental values only to some extent. For the case of neon, a calculation based on the many-body perturbation approach was performed in the optical transitions $2p^5 3s \rightarrow 2p^5 3p$ [29]. Although it reproduces fairly well the measured isotope shifts, the results are not accurate enough to reveal the small field shifts.

We separate the field shift and the mass shift in Eq. (8) using an empirical method. It is based on the knowledge of the differences between the mean square nuclear charge radii of the stable isotopes,

$$\begin{aligned}\delta\langle r^2\rangle^{20,21} &= -0.233(16)[23]\,\text{fm}^2 \qquad \text{and} \\ \delta\langle r^2\rangle^{20,22} &= -0.310(16)[31]\,\text{fm}^2. \end{aligned} \tag{10}$$

The quoted values were deduced from the model-dependent nuclear charge radii derived from muonic atom spectra as compiled by Fricke *et al.* [30]. Thus, we have two independent values for $\delta\langle r^2\rangle^{20,A}$ corresponding to two experimental isotope shifts, $\delta\nu_{\rm exp}^{20,A}$, from which in principle both the mass shift constant $(M_n + M_s)$ and the electronic factor F can be determined using Eq. (8). However, such a procedure would give too large uncertainties. Making use of the fact that the electronic factor F is known independently, we adopt this value and extract from the known radii only the mass shift constant.

Using this procedure we also take advantage of the feature that systematic uncertainties of the isotope shift arising from the high-voltage calibration cancel out in the evaluation of mean square charge radii differences. These uncertainties have in very good approximation the same mass dependence as the mass shift [12]. They can be expressed in terms of two parameters, k_U and $k_{\Delta U}$, accounting for deviations of the measured acceleration voltage U and postacceleration voltage differences ΔU from their true values:

$$\epsilon(\delta\nu^{20,A}) \approx (k_U + k_{\Delta U})\frac{m_A - m_{20}}{m_A m_{20}}. \tag{11}$$

By adding this as a correction to Eq. (8), we obtain for the experimentally determined isotope shift:

$$\delta\nu_{\rm exp}^{20,A} = F\,\delta\langle r^2\rangle + (M_n + C)\frac{m_A - m_{20}}{m_A m_{20}}, \tag{12}$$

where

$$C = M_s + k_U + k_{\Delta U} \tag{13}$$

can be treated as an effective specific mass shift constant. Thus a fit of the isotope shifts according to Eq. (8), using the known reference radii and the field shift factor as given by Eq. (9), yields this constant modified by the effect of systematic voltage deviations and leaves the field shifts unaffected. We obtain

$$C = 95.43[42]\,\text{GHz u}. \tag{14}$$

The error in (14) is from the uncertainties of the muonic radii and the semiempirical electronic factor.

The dominating experimental systematic errors arising from the voltage measurements have to be included only if we identify the quantity C with the specific mass shift constant M_s. These are obtained by varying the correction factors k_U and $k_\Delta U$ within the limits given by the known calibration uncertainties of U and ΔU, yielding

$$M_s^{\rm exp} = 95.43[80]\,\text{GHz u}. \tag{15}$$

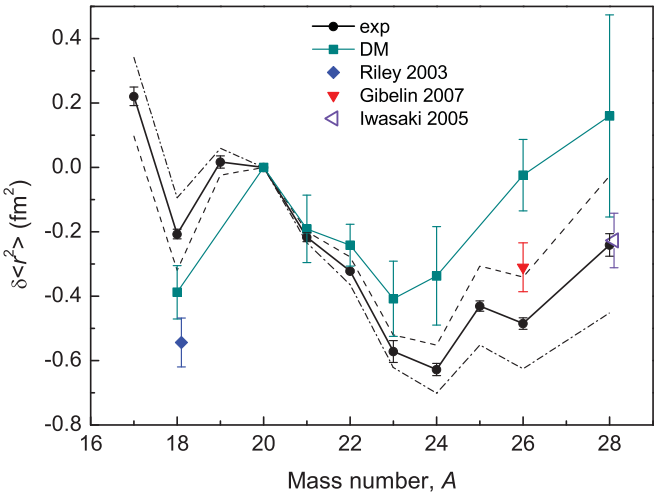

FIG. 5. (Color online) Changes in mean square charge radii $\delta\langle r^2\rangle$ for $^{17-28}$Ne, with respect to ^{20}Ne (exp). The error bars represent statistical errors; systematic calibration uncertainties are indicated by upper (dashed) and lower (dashed-dotted) boundary lines. Droplet model predictions (DM) are based on quadrupole deformation from experimental $B(E2)$ values [31] and spectroscopic quadrupole moments. Predictions from recently published $B(E2)$ values are shown separately (see Fig. 7; for the droplet model, see Sec. IV B).

In conclusion, uncertainties of the voltage calibration do not influence the field shift which is separated for each isotope from the experimental isotope shift by means of Eq. (12), independently of a deviation of C from the real mass shift constant. The values of $\delta\langle r^2\rangle^{20,A}$ compiled in Table II have been derived using the scaling factors (9) and (14).

The accuracy of the changes in mean square charge radii $\delta\langle r^2\rangle$ derived from measured isotope shifts is determined by: (i) the errors of the individual measurements, which are shown in parentheses and arise from the statistical errors of the isotope shifts; (ii) the systematic uncertainty in the field shift from the evaluation of the effective specific mass shift represented by the scaling factor (14); (iii) the error assumed for the electronic factor F from Eq. (9) which relates the nuclear parameters to optical frequencies. Errors from the measured values of atomic masses [9,25] are largely negligible. Total systematic errors of $\delta\langle r^2\rangle^{20,A}$ are presented in Table II (square brackets). The data of $\delta\langle r^2\rangle^{20,A}$ collected in Table II are plotted in Fig. 5, with statistical errors as error bars and systematic errors as contour lines enclosing the permissible range of slopes. It is important to note that nuclear structure effects show up as relative changes of $\delta\langle r^2\rangle$ between the isotopes, independently of the general slope.

IV. DISCUSSION

Beyond the statistical errors the evolution of the mean square charge radii of the neon isotopes as a function of neutron number (Fig. 5) is characterized by fluctuations at the lower end of the *sd* shell, large radii for the deformed isotopes around the stable ^{20}Ne and a pronounced minimum in the middle of the shell around ^{24}Ne. Toward the upper end of the *sd* shell the radii increase again, probably indicating the influence of deformation, which is related to the occupation of intruder states from the $f_{7/2}$ shell in the $N = 20$ region. The behavior is similar to that observed in the neighboring element sodium (see [6]) where Campi *et al.* [32] showed by deformed Hartree-Fock calculations that the particular features of binding energies and radii in this region can be understood in terms of deformation effects. For this reason, we will consider how deformation shows up along the neon isotopes in the *sd* shell.

A. Nuclear charge radii and quadrupole deformation

1. Even-even neon isotopes

An overview of the deformation properties in the full range of $18 \leqslant A \leqslant 28$ can be gained from a compilation of the first 2^+ excitation energies $E(2_1^+)$ and the ratios $E(4_1^+)/E(2_1^+)$, in combination with reduced transition probabilities $B(E2; 0_1^+ \rightarrow 2_1^+)$ and deformation parameters β_2 deduced from them (see Sec. IV B). This is shown in Table III and in Figs. 6 and 7. The generally large $B(E2)$ values indicate a collective nature for all these nuclei.

For ^{18}Ne at the $N = 8$ shell closure there are conflicting results of $B(E2)$ values from conventional lifetime measurements [31,36] and recently from intermediate energy Coulomb excitation cross sections [36,39]. Both clearly indicate a deformation minimum as expected for the magic neutron number, but with the intermediate energy value this appears somewhat more pronounced.

The deformation properties of stable ^{20}Ne, which we use as a reference isotope for the measured changes in mean square charge radii, are well known and have long been discussed (see [40] and references therein). This nucleus is specified as a good rotor with large quadrupole deformation. The ^{20}Ne ground state is associated with a dominant cluster structure of a ^{16}O core plus an α particle [9,41,42]. Within this model it is obvious that the α particle outside the spherical core gives rise to an intrinsically deformed charge distribution. Similarly,

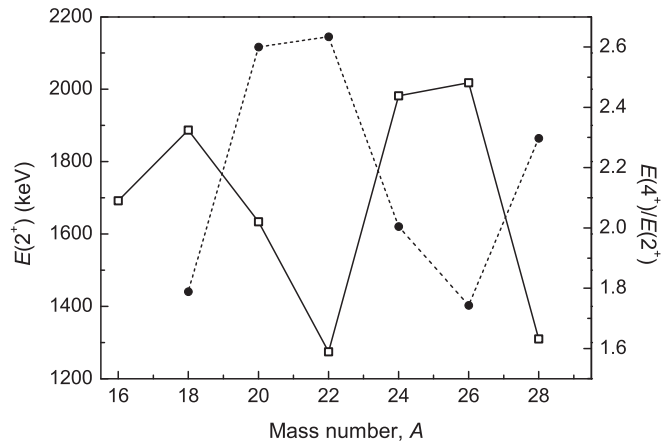

FIG. 6. Energies $E(2_1^+)$ of the first excited states (open squares) and energy ratios $E(4_1^+)/E(2_1^+)$ of the lowest 4^+ and 2^+ excited states (solid circles) for even-even Ne isotopes.

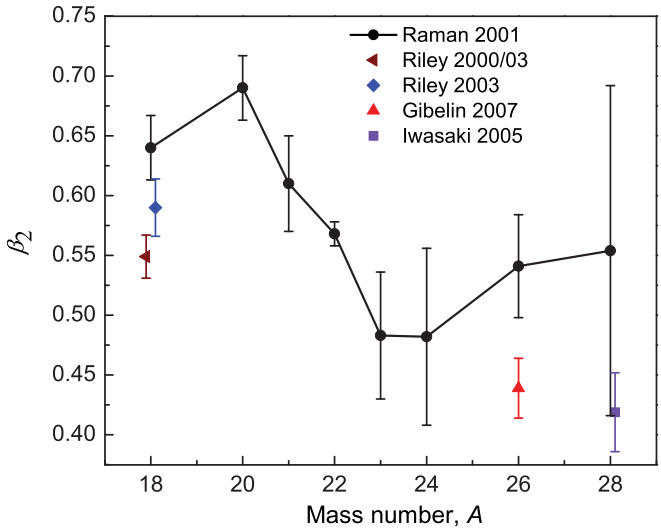

FIG. 7. (Color online) Experimental β_2 deformation parameters versus atomic number (solid circles) from $B(E2)$ values [31] or from spectroscopic quadrupole moments [8] obtained as described in Sec. IV B. Deformations from more recently published $B(E2)$ values for ^{18}Ne (Riley *et al.* [36]), ^{26}Ne (Gibelin *et al.* [37]), and ^{28}Ne (Iwasaki *et al.* [38]) are shown separately.

^{22}Ne with two additional neutrons is strongly deformed [40]. According to experimental data [31] and several shell-model or mean-field calculations (see Sec. IV C and [44]) the isotopes around ^{20}Ne and ^{22}Ne belong to the most deformed nuclei in the sd shell. These features explain why they have the largest charge radii.

A deformation minimum is approached for ^{24}Ne in the middle of the sd shell [31] corresponding to the closure of the $d_{5/2}$ subshell. Accordingly, ^{24}Ne has the smallest charge radius of all neon isotopes. It is worth noting that for ^{24}Ne as well as for ^{26}Ne the energy ratios $E(4^+)/E(2^+)$ indicate that collectivity originates from vibrations rather than rotations (see Table III).

For ^{26}Ne and ^{28}Ne the excitation energies and $B(E2)$ values of the lowest $J^\pi = 2^+$ state were first measured [35] via intermediate energy Coulomb excitation. The $E(2_1^+)$ value of ^{26}Ne is consistent with the sd-shell model description [43,45] which predicts that $E(2_1^+)$ remains almost constant for $N =$ 16–20. However, for ^{28}Ne the experimental value of $E(2_1^+)$ drops considerably and is in good agreement with calculations in an extended sd-fp model space [46]. The $B(E2)$ value of ^{28}Ne was found to be correspondingly large. On the other hand, more recent and more accurate $B(E2)$ values for both isotopes [37,38] are considerably smaller, suggesting much smaller deformation for ^{28}Ne than expected from the 2_1^+ energy. So far the inconsistencies remain unexplained, but they may be from differences in the method of extracting $B(E2)$ values from 2^+ excitation cross sections.

Additional information on the level structure of ^{26}Ne and ^{28}Ne was obtained from in-beam γ-ray spectroscopy using fragmentation reactions [34,47], confirming the 2^+ and also providing 4^+ excitation energies. A shell-model interpretation suggests that the interaction between coexisting normal and intruder configurations significantly perturbs the energy of the 2_1^+ state in ^{28}Ne, thus producing large quadrupole deformation. Reaction studies on ^{28}Ne (see, e.g., [48,49]) are also consistent with the presence of fp-shell configurations at low excitation energy, meaning that for $Z = 10$ the neutron sd-fp shell gap starts to vanish already at $N = 18$. This can also explain the observed increase in the mean square charge radius toward ^{28}Ne. For ^{30}Ne the first excited state was found at about 800 keV [50], lower than for any other Ne isotope, which strengthens all other evidence that $N = 20$ is not magic for $Z = 10$.

2. *Odd-A neon isotopes*

The deformation properties of the investigated odd-A neon isotopes ^{19}Ne, ^{21}Ne, ^{23}Ne, and ^{25}Ne are supported by their spins, which contradict the spherical shell model. Assuming deformed nuclei, the single-particle levels can be described within the Nilsson model. The most probable Nilsson configurations accounting for the experimental spin-parity values are given in Table IV. For ^{21}Ne and ^{23}Ne the spectroscopic quadrupole moments Q_s have been measured by laser spectroscopy [8]. From these the intrinsic quadrupole moments Q_0 and β_2 are obtained via the strong-coupling projection formula which is expected to hold in the case of axially symmetric and strongly deformed nuclei (Table IV).

3. *Shell structure in the neon isotope chain*

The known Ne isotopes span the full neutron sd shell and cross the magic numbers $N = 8$ and $N = 20$. However, the

TABLE III. Comparison of $J^\pi = 2^+$ and 4^+ level energies and $B(E2; 0^+ \to 2^+)$ values for even-A Ne isotopes. Deformation parameters are derived from experimental data using droplet model (DM) formulas for $Q_0 = \sqrt{16\pi/5 \times B(E2)}$ (see Sec. IV B). Values for $^{18-24}$Ne are taken from [31,33] and for ^{26,28}Ne partly from [34,35]. More recent alternative $B(E2)$ values are given for ^{18}Ne [36], ^{26}Ne [37], and ^{28}Ne [38].

	^{18}Ne	^{20}Ne	^{22}Ne	^{24}Ne	^{26}Ne	^{28}Ne	^{30}Ne
$E(2^+)$ (keV)	1887	1634	1275	1982	2024	1293	791
$E(4^+)$ (keV)	3376	4248	3357	3962	3523	3000	
$E(4^+)/E(2^+)$	1.79	2.60	2.63	2.00	1.74	2.32	
$B(E2; 0^+ \to 2^+)(e^2\text{fm}^4)$	269(26)	340(30)	230(10)	170(60)	228(41)	269(136)	
	222(20)				141(18)	132(23)	
β_2(DM)	0.640(27)	0.690(27)	0.568(10)	0.482(74)	0.541(43)	0.554(138)	
	0.590(24)				0.439(25)	0.419(33)	

TABLE IV. Measured spin and assigned parity [8] with corresponding Nilsson configurations for the odd-A Ne isotopes. Spectroscopic (Q_s) and intrinsic (Q_0) quadrupole moments for isotopes with spin $I > 1/2$. For comparison Q_0 deduced from rotational level lifetimes [51] is shown for ^{21}Ne. Deformation parameters were calculated from Q_0 using droplet model formulas (see Sec. IV B).

A	I^π	Nilsson state	Q_s (b)	Q_0 (b)	β_2(DM)
17	$1/2^-$	$1/2^-[101]$			
19	$1/2^+$	$1/2^+[220]$			
21	$3/2^+$	$3/2^+[211]$	0.1029(75)	0.515(38) 0.55(6)	0.610(40)
23	$5/2^+$	$5/2^+[202]$	0.145(6)[12]	0.406(50)	0.483(53)
25	$1/2^+$	$1/2^+[211]$			

shell structure derived from stable nuclides changes further away from stability, and as a result some traditional magic numbers disappear and new magic numbers take their place.

The cancellation of the magic neutron numbers $N = 8$ and $N = 20$ in exotic light nuclei and the appearance of new magic numbers such as $N = 14$ or $N = 16$ is widely discussed in the literature from the experimental and theoretical point of view (see [52,53] and references therein). The $N = 20$ shell gap between $d_{3/2}$ and $f_{7/2}$ (and $p_{3/2}$) orbits was the first gap shown to be weakened far from stability [5,54]. The first evidence from mass measurements of Na [55] and Mg [56] isotopes in this deformation region named the "island of inversion," was strengthened by multiple other observables such as excitation energies and transition strengths, or spins and electromagnetic moments. In the last decade it was shown that the disappearance of $N = 20$ magicity is accompanied by the emergence of a new magic number $N = 16$, which is from the upward shift in the neutron $d_{3/2}$ orbital with the proton number approaching $Z = 8$ [46,57]. Experimental evidence was found in the systematics of neutron separation energies and interaction cross sections [58]. Further studies were based on neutron-removal reactions mainly in the neutron-rich oxygen isotopes up to the drip line at ^{24}O (see [53]). Because of the separated position of the neutron $s_{1/2}$ orbital between $d_{5/2}$ and $d_{3/2}$, also $N = 14$ was discussed as a possible shell closure [59].

In the development of charge radii, shell closures manifest themselves as minima superimposed on the continuous increase of $\langle r^2 \rangle$ as a function of the neutron number N. This gives rise to the characteristic slope changes (kinks) at magic neutron numbers, which are observed at all neutron shell closures with $N \geqslant 28$ [60]. For the neon radii a distinct minimum is observed for ^{18}Ne at the classical shell closure $N = 8$. However, this appears as a local effect, which does not influence the trends of the isotopes in the neighborhood because the proton halo component develops in ^{17}Ne (see Sec. IV C and [9]) and strong deformation sets in as soon as neutrons are occupying the *sd* shell. In contrast to the behavior expected for a shell closure, the radii increase steeply when approaching $N = 20$. This supports the evidence for a breakdown of the $N = 20$ magic number, which was already discussed above. Deformed $2p$-$2h$ states intrude below the normal spherical states forming the island of inversion, and several experiments have consistently indicated that already ^{28}Ne with $N = 18$ belongs to this island.

In the middle of the *sd* shell, the development of the radii around the minimum observed at $N = 14$ (see Fig. 5) shows the characteristic features of a magic shell closure. A similar behavior is observed in the sodium radii [6]. This neutron number corresponds to a completed $d_{5/2}$ subshell, suggesting an increased $N = 14$ gap between $d_{5/2}$ and $s_{1/2}$. One would expect that this is associated with a deformation minimum for ^{24}Ne as it is shown in tabulated data [31] on $B(E2)$ values. However, these are only partly consistent with the results of recent experiments [37,38] in which intermediate-energy Coulomb excitation cross sections have yielded decreasing $B(E2)$ values up to ^{28}Ne. On the other hand, the appearance of an increased subshell gap at $N = 14$ and/or $N = 16$ is in line with observations of unusual stability reflected in nuclear masses. The evidence for a shell closure is found in a significant drop of the two-neutron separation energy above the magic neutron number. Surprisingly, in the Ne isotopes this occurs for the odd neutron number $N = 15$, and a possible reason for such a behavior was discussed in an early conference report [61]. A further exception from the usual behavior at shell closures is that the steep decrease of two-neutron binding energies continues over three neutron numbers, up to $N = 18$. Based on this, further investigations [62] have again advocated the dominance of a shell gap at $N = 16$.

The 2_1^+ energies of both isotopes, ^{24}Ne and ^{26}Ne, are even larger than for ^{18}Ne at the $N = 8$ shell closure. Together with all other aspects this probably means that $N = 14$ and $N = 16$ are involved in the shell closure effect observed in the middle of the traditional *sd* shell. The energy ratio $E(4^+)/E(2^+)$ decreases considerably above $N = 12$, reaching a minimum at $N = 16$ (see Table III and Fig. 6) which is slightly lower than the ratio of 1.79 observed for ^{18}Ne. While these values indicate close-to-spherical vibrational nuclei, the $E(4^+)/E(2^+)$ ratios for ^{20,22}Ne are closer to 3.33 as found for deformed rotors.

The question whether $N = 14$ or 16 should be considered as a magic neutron number depends sensitively on the position of the $2s_{1/2}$ level between $1d_{5/2}$ and $1d_{3/2}$ as a function of the proton number Z. These neutron numbers separate $j = l + 1/2$ and $j = l - 1/2$ orbits in analogy to the magic numbers in the heavier-mass region. At least for neon with $Z = 10$ the behavior of radii slightly favors $N = 14$ as being "more magic" than $N = 16$.

B. Droplet model nuclear charge radii of neon isotopes

Features of deformation are present in the neon isotopes throughout the *sd* shell, and we can try to attribute the observed changes in nuclear charge radii to known deformation properties of the individual isotopes. The β_2 values in [31] were calculated from $B(E2)$ values using the first-order formula $\beta_2 = (4\pi/3ZR_0^2)[B(E2;0^+ \rightarrow 2^+)/e^2]^{1/2}$. However, this limitation to the lowest order in β_2 leads to overestimated deformation values. This is especially important for large deformations, where higher-order terms contribute substantially to the quadrupole moment. In addition, the assumption of a spherical radius $R_0 = 1.2A^{1/3}$ fm is not a good approximation for light nuclei. In this paper the deformation parameters and

radii were calculated using the droplet model [63] according to which the dependence of the intrinsic quadrupole moment Q_0 on the quadrupole deformation parameter $\alpha_2 = (5/4\pi)^{1/2}\beta_2$ is given by

$$Q_0 = \frac{6}{5} Z R_Z{}^2 \left(\alpha_2 + \frac{4}{7}\alpha_2{}^2 - \frac{1}{7}\alpha_2{}^3 + \cdots\right) + \frac{48}{157} C' Z R_Z{}^2 \left(\alpha_2 + \frac{6}{7}\alpha_2{}^2 - \frac{4}{5}\alpha_2{}^3 - \cdots\right). \quad (16)$$

Here R_Z is the effective sharp radius of the proton distribution and C' is the Coulomb redistribution correction. In the evaluation of β_2 from Eq. (16) we have included terms up to the third power in α_2 and omitted terms accounting for higher-order deformation.

The mean square charge radii are equally influenced by static and dynamic deformation of the nuclear charge distribution. Both of them are inherently included [64] in the effective β_2 values (Table III)—literally expressed as $\sqrt{\langle\beta_2{}^2\rangle}$—which are deduced for the even isotopes from experimental $B(E2; 0_1^+ \rightarrow 2_1^+)$ values. For the odd-A isotopes, the values of Q_0 and β_2 shown in Table IV were deduced from measured spectroscopic quadrupole moments and they represent static deformation only. The trend of these empirical deformation parameters β_2 according to Eq. (16) is displayed in Fig. 7.

With deformations from $B(E2)$ values and from spectroscopic quadrupole moments the droplet-model description [63] of mean square charge radii,

$$\langle r^2\rangle^A = \frac{3}{5} R_Z{}^2 \left(1 + \alpha_2{}^2 + \frac{10}{21}\alpha_2{}^3 - \cdots\right) + \frac{12}{175} C' R_Z{}^2 \times \left(1 + \frac{14}{5}\alpha_2{}^2 + \frac{28}{15}\alpha_2{}^3 - \cdots\right) + 3b^2, \quad (17)$$

where b accounts for the surface diffuseness, can be used to make a prediction for $\delta\langle r^2\rangle^{20,A}$ along the chain of isotopes. The result is included in Fig. 5. Apart from a somewhat different general slope, which is determined by the droplet model coefficients adjusted to ground-state masses over the whole nuclide chart, the radii obtained from such a simple collective picture reproduce the experimental data quite well. The description of irregularities in the charge radii in terms of a single shape parameter appears to be a valid approach. This is surprising in a region where single-particle orbitals and clustering are supposed to dominate the nuclear properties. It is in contrast to the behavior of other light nuclear systems such as the Ca and Ar isotopes [12] in the neighborhood of the $Z = 20$ shell closure, where deformation is small and single-particle contributions dominate over collective properties. Similarly, for heavier systems it was found that the semiempirical droplet description is most suitable in regions of strong deformation.

We note that all quadrupole moments Q_0 and thus all deformation parameters β_2 were assumed to be positive, although the sign cannot be determined from $B(E2)$ values alone. The leading terms in Eqs. (16) and (17) are independent of this sign assumption. However, by including α, α^2, and α^3 terms, the picture can change to some extent, if mainly surface vibrations or oblate deformations are responsible for the $B(E2)$ values. As suggested by some theoretical calculations discussed in the following section, this may be the case in the midshell region around ^{24}Ne and ^{26}Ne.

C. Theoretical models

There are several theoretical studies providing absolute charge radii of neon isotopes. To compare these calculations with our data it is most instructive to deal not only with differences, but with total rms charge radii derived using as a reference the value measured for ^{20}Ne, $R_c = 3.006(5)$ fm [30].

The most recent calculations using the fermionic molecular dynamics (FMD) model concentrate on specially $^{17-22}$Ne [9,65]. This approach shows a remarkable agreement with experimental charge radii because it includes both shell and clustering effects. It also reproduces very well the experimental one- and two-neutron separation energies and $B(E2)$ values. The increase of the charge radius from ^{18}Ne to ^{17}Ne at the proton drip line is related to the development of a halo component in the wave function with a proton s^2 occupation probability changing from 15% to 40%. Relative to ^{18}Ne, the radii of $^{19-22}$Ne are again larger but decrease with increasing neutron number. This is from cluster configurations of the nucleons outside the doubly magic ^{16}O core, which in the simplest case of ^{20}Ne form just an α cluster. These configurations are related to the known deformation decreasing toward ^{24}Ne. Calculations beyond ^{22}Ne are not envisaged at the moment because of a very long computational time increasing with the number of nucleons and possible cluster components outside the ^{16}O core.

The binding energies, deformations, and charge radii of neon isotopes have also been calculated using the more classical mean-field approach. Below, we divide the discussion into models devoted to only even-even isotopes and those devoted also to odd-mass isotopes.

The properties of even-A neon isotopes have been addressed using several mean-field models. To these belong approaches optimized for light isotopic chains, such as the deformed relativistic mean-field approach (RMF) with BCS theory for pairing correlations [66], deformed Hartree-Fock (HF) plus BCS calculations using Skyrme interaction [43], or very recent calculations within a relativistic Hartree-Fock-Bogoliubov (RHFB) model [67]. The radii and deformations obtained with these models are plotted with experimental data in Fig. 8. The former calculations give an unrealistically large charge radius of ^{18}Ne at the $N = 8$ shell closure, but reproduce well the radii minimum at ^{24,26}Ne. The HF plus BCS calculations result in generally larger radii and smoother changes, with only a shallow minimum at ^{24,26}Ne and a ^{18}Ne value again without indication of a shell closure effect. The most recent RHFB model, with the PKO3 interaction including explicitly the pion field, agrees with most of the experimental radii: It predicts minima for $N = 8$ and $N = 14$, large radii for ^{20,22}Ne, and a linear increase from $N = 14$ toward $N = 20$ and beyond. Deformations on the mean-field level are predicted to be appreciable only in the lower part of the sd shell, in particular for the stable ^{20}Ne and ^{22}Ne. Note that for soft nuclei, where configuration mixing plays an important role, the agreement with experimental β_2 derived from $B(E2)$ values is expected to be less good.

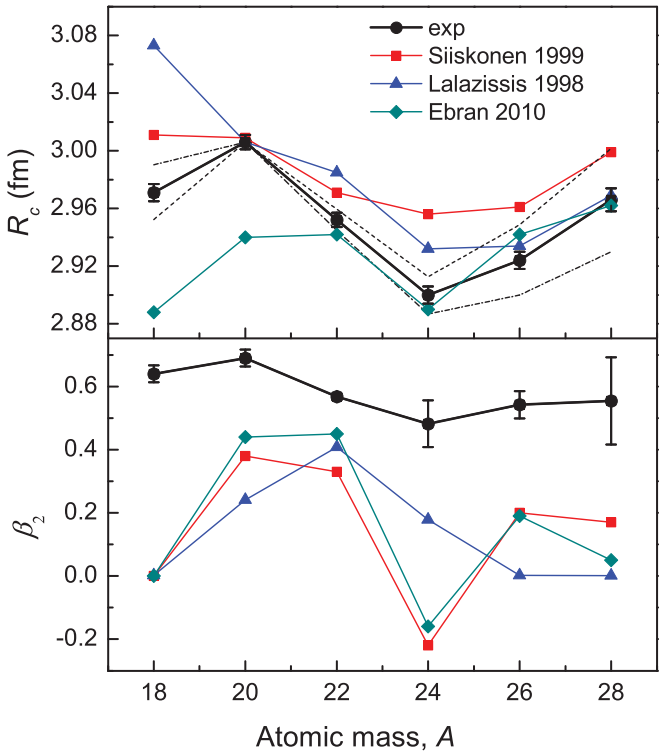

FIG. 8. (Color online) (a) Rms nuclear charge radii R_c and (b) deformation parameters β_2 of even-even Ne isotopes (exp), compared to theoretical predictions of Siiskonen *et al.* [43], Lalazissis *et al.* [66], and Ebran *et al.* [67]. For the radii, the error bars represent statistical uncertainties, while systematic error limits are given by the dashed and dotted lines.

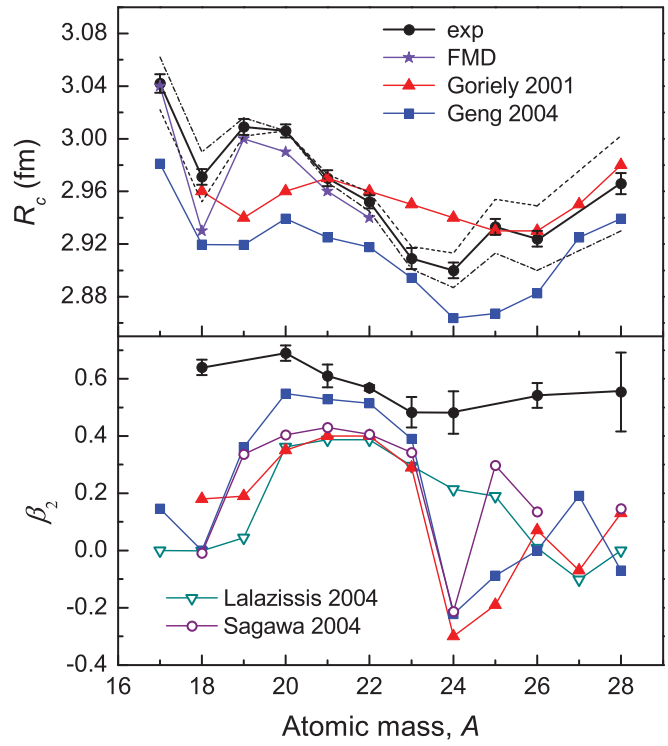

FIG. 9. (Color online) (a) Rms nuclear charge radii R_c and (b) deformation parameters β_2 of all investigated Ne isotopes (exp), compared to theoretical predictions of Goriely *et al.* [69] and Geng *et al.* [68]. Additional calculated β_2 values of Lalazissis *et al.* [71] and Sagawa *et al.* [70] are shown in (b). The radii of the lighter isotopes $^{17-22}$Ne are best described by the recent FMD approach [9]. Error bars of experimental radii represent statistical uncertainties, whereas systematic error limits are given by the dashed and dotted lines.

Among the models addressing also odd-mass isotopes, deformed relativistic mean-field theory plus delta-function interaction for pairing [68] was used to calculate the neon charge radii along with other ground-state properties of light nuclei in the $10 \leqslant Z \leqslant 18$ region. The results reproduce qualitatively the progression of radii including the local minima for ^{18}Ne and ^{24,26}Ne with an increase toward ^{17}Ne and ^{28}Ne, however all absolute radii are somewhat too small. On the other hand, deformed Hartree-Fock plus BCS calculations, performed for all nuclei in the nuclear chart [69], reproduce on average better the absolute radii, but miss characteristic features such as the large radii of ^{19,20}Ne and a pronounced minimum at ^{24}Ne, while also showing an increase from ^{25}Ne to ^{28}Ne. The radii calculated with the above models are compared to our data in Fig. 9(a). The deformations from both models, and from additional calculations using a deformed Skyrme Hartree-Fock model [70] and a relativistic Hartree-Bogoliubov model with Gogny interaction [71], fit to those obtained for just the even-even isotopes. Strong deformation is predicted to exist in the range of ^{19}Ne or ^{20}Ne to ^{23}Ne. Details of this comparison are shown in Fig. 9(b).

It is evident that the absolute radii as well as the characteristic trend with a minimum close to the middle of the *sd* shell are reproduced reasonably well by the models. However, all structural details including the maximum just above $N = 8$ and the midshell minimum are less pronounced than in the experimental data. Already without the inclusion of a reduced *sd-pf* shell gap driving deformation, the models predict an increase of the radii toward ^{28}Ne. This calls for theoretical calculations of radii including explicitly the shell structure around $N = 20$ in a *sdpf* shell-model basis, as they have been performed for the nuclear level structure and the moments [34,46].

In respect to β_2 values, most theoretical approaches reproduce the known deformation properties of the nuclei between ^{19}Ne and ^{23}Ne, predict a near-spherical shape for ^{24}Ne, and give different values of small deformation for the more neutron-rich isotopes. Both ^{18}Ne and ^{30}Ne at the traditional $N = 8$ and $N = 20$ shell closures are predicted to be spherical. In contrast to conventional calculations, the Monte Carlo shell model with a reduced *sd-pf* shell gap [46] gives realistic $B(E2)$ values corresponding to large deformation for the neutron-rich ^{26}Ne and ^{28}Ne. Generally the theoretical β_2 values are much smaller than the experimental ones calculated from $B(E2)$. Here one has to keep in mind that experimental and theoretical values of β_2 depend on model assumptions (see Sec. IV A), and that experimental $B(E2)$ values contain dynamic in addition to static deformations [64], which both also contribute to the mean square charge radii.

Neither the $B(E2)$ values nor the mean square charge radii are sensitive to the sign of β_2 values. Most theoretical approaches predict oblate shapes for the ground states of ^{24}Ne

and ^{25}Ne in the middle of the *sd* shell. This is explained with the fully occupied $d_{5/2}$ orbital at $N = 14$ favoring oblate deformation [44]. Shape coexistence with very flat and nearly degenerate prolate and oblate energy minima is also found for the more neutron-rich isotopes [70]. In this context it would be interesting to measure the spectroscopic quadrupole moment of ^{27}Ne for which different shapes are predicted.

V. CONCLUSION

We have performed laser spectroscopy measurements on $^{17-28}$Ne for the determination of isotope shifts and hyperfine structures. The present results on isotope shifts, including previously published data on $^{17-22}$Ne [9], give insight into the development of mean square charge radii from the proton drip line over the $N = 8$ shell closure to the neighborhood of $N = 20$. Spins and nuclear moments of ^{17}Ne, ^{23}Ne, and ^{25}Ne, obtained from the analysis of hyperfine structure for the odd-A isotopes, were published separately [8]. Known radii of the stable isotopes $^{20-22}$Ne [30] were used to isolate the small nuclear volume (field) shifts from the isotope shifts dominated by mass shifts, which remained a major problem in the analysis of the early laser spectroscopy data on sodium [6,7]. Moreover, this procedure eliminates systematic errors of the evaluated radii arising from the large Doppler shifts [12].

The short-lived isotopes far from stability became accessible from the application of an efficient resonance detection scheme based on collisional ionization and ion counting via the β decay [11,12]. This also avoids background from laser light and from ion beam contamination with stable isobars. The determination of small field shifts in the low-Z element neon requires high accuracy of the isotope shift measurements, typically about 1 MHz, which in collinear laser spectroscopy implies a very good calibration of the beam energy. This was achieved by verifying the acceleration voltage for which two known transition frequencies in ^{20}Ne, measured with collinear and anticollinear beams and thus Doppler-shifted in opposite directions, coincide at the same laser frequency.

The comparison between experimentally determined changes in charge radii and values calculated from the droplet model [63] using empirical β_2 deformation values shows a clear correlation between both quantities. The well-known deformation properties around the stable isotopes $^{20-22}$Ne and the $N = 8$ shell closure at ^{18}Ne are clearly reflected in the radii. Below, the proton drip line is reached with the proton halo candidate ^{17}Ne. Its properties have been discussed in detail in our previous papers [8,9], advocating the development of a proton halo component, but no well-developed halo.

In the region of neutron-rich isotopes, close to $N = 20$, the large neutron excess affects the spin-orbit and the proton-neutron interaction, thereby changing the order of filling the nucleon orbits. The disappearance of the $N = 20$ shell gap, driving deformation at a classical magic number, was suggested long ago [5,54]. Recent experimental [34,35,47] and theoretical [46] studies of low-lying states in ^{26}Ne and ^{28}Ne provide evidence that ^{28}Ne with two neutrons less than the traditional $N = 20$ shell closure is located in the island of inversion. Although this is partly questioned by recent results on $B(E2)$ values, the increase of nuclear radii toward $N = 20$, beyond the minimum at $N = 14$, suggests a magic number in the middle of the *sd* shell and appreciable deformation already for ^{28}Ne.

The nuclear radii presented in this paper range into exotic regions of the *sd* shell. Together with the earlier published nuclear moments [8] they show a diversity of nuclear structure phenomena occurring for Ne isotopes between $N = 7$ and 18. These can be explained by the appropriate theoretical models, but a coherent description of different nuclei and observables is still pending.

ACKNOWLEDGMENTS

We thank H. Scheit, D. Lunney, and E. Khan for valuable discussions. This work was supported by the German Federal Ministry for Education and Research (BMBF), Contract Nos. 06 MZ 866 I and 06 MZ 962 I, by the Belgian Research Foundation-Flanders, and by the European Union in the framework of the HPRI program. Special thanks are due to the Alexander-von-Humboldt Foundation for supporting the research visits of K. Marinova to Mainz and CERN. We also thank the ISOLDE technical group for its assistance.

[1] B. Jonson, Phys. Rep. **389**, 1 (2004).
[2] M. J. G. Borge *et al.*, Phys. Lett. B **317**, 25 (1993).
[3] M. V. Zhukov and I. J. Thompson, Phys. Rev. C **52**, 3505 (1995).
[4] W. von Oertzen, M. Freer, and Y. Kanada En'yo, Phys. Rep. **432**, 43 (2006).
[5] E. K. Warburton, J. A. Becker, and B. A. Brown, Phys. Rev. C **41**, 1147 (1990).
[6] F. Touchard *et al.*, Phys. Rev. C **25**, 2756 (1982).
[7] G. Huber *et al.*, Phys. Rev. C **18**, 2342 (1978).
[8] W. Geithner *et al.*, Phys. Rev. C **71**, 064319 (2005).
[9] W. Geithner *et al.*, Phys. Rev. Lett. **101**, 252502 (2008).
[10] W. Geithner *et al.*, Hyperfine Interact. **127**, 117 (2000).
[11] R. Neugart, Hyperfine Interact. **24–26**, 159 (1985).
[12] A. Klein, B. A. Brown, U. Georg, M. Keim, P. Lievens, R. Neugart, M. Neuroth, R. E. Silverans, and L. Vermeeren, Nucl. Phys. A **607**, 1 (1996).
[13] E. Kugler, Hyperfine Interact. **129**, 23 (2000).
[14] R. Neugart, W. Klempt, and K. Wendt, Nucl. Instrum. Methods B **17**, 354 (1986).
[15] NIST Atomic Spectra Database, NIST Standard Reference Database **78** (National Institute of Standards and Technology, 2008) [http://physics.nist.gov/PhysRefData/ASD/].
[16] K. Blaum, W. Geithner, J. Lassen, P. Lievens, K. Marinova, and R. Neugart, Nucl. Phys. A **799**, 30 (2008).
[17] O. Poulsen, Nucl. Inst. Meth. **202**, 503 (1982).
[18] P. Zhao, J. Opt. Soc. Am. B **4**, 644 (1987).
[19] P. Juncar and J. Pinard, Rev. Sci. Instr. **53**, 939 (1982).
[20] Ch. Belfrage, P. Grafström, S. Kröll, and S. Svanberg, Phys. Scr. **27**, 367 (1983).
[21] G. Guthöhrlein and L. Windholz, J. Optics Research **2**, 171 (1994).
[22] E. Konz, T. Kraft, and H.-G. Rubahn, Appl. Opt. **31**, 4995 (1992).

[23] V. I. Odintsov, Opt. Spectrosc. **18**, 205 (1965).
[24] A. C. Mueller, F. Buchinger, W. Klempt, E. W. Otten, R. Neugart, C. Ekström, and J. Heinemeier, Nucl. Phys. A **403**, 234 (1983).
[25] G. Audi, A. H. Wapstra, and C. Thibault, Nucl. Phys. A **729**, 337 (2003).
[26] Gö. Basar, Gü. Basar, S. Büttgenbach, S. Kröger, and H.-D. Kronfeld, Z. Phys. D **39**, 283 (1997).
[27] H. Kopfermann, *Nuclear Moments* (Academic Press, New York, 1958).
[28] M. Keim, E. Arnold, W. Borchers, U. Georg, A. Klein, R. Neugart, L. Vermeeren, R. E. Silverans, and P. Lievens, Nucl. Phys. A **586**, 219 (1995).
[29] S. Ahmad, J. Phys. B **18**, 3457 (1985).
[30] G. Fricke, C. Bernhardt, K. Heilig, L. A. Schaller, L. Schellenberg, E. B. Shera, and C. W. de Jager, At. Data Nucl. Data Tables **60**, 177 (1995).
[31] S. Raman, C. W. Nestor Jr., and P. Tikkanen, At. Data Nucl. Data Tables **78**, 1 (2001).
[32] X. Campi, H. Flocard, A. K. Kerman, and S. Koonin, Nucl. Phys. A **251**, 193 (1975).
[33] R. B. Firestone and V. S. Shirley, *Table of Isotopes*, 8th ed. (Wiley, New York, 1996).
[34] M. Belleguic *et al.* , Phys. Rev. C **72**, 054316 (2005).
[35] B. V. Pritychenko *et al.*, Phys. Lett. B **461**, 322 (1999).
[36] L. A. Riley *et al.*, Phys. Rev. C **68**, 044309 (2003).
[37] J. Gibelin *et al.* Phys. Rev. C **75**, 057306 (2007).
[38] H. Iwasaki *et al.*, Phys. Lett. B **620**, 118 (2005).
[39] L. A. Riley, P. D. Cottle, M. Fauerbach, T. Glasmacher, K. W. Kemper, B. V. Pritychenko, and H. Scheit, Phys. Rev. C **62**, 034306 (2000).
[40] A. Bohr and B. R. Mottelson, *Nuclear Structure*, Vol. II (*Nuclear Deformations*) (Benjamin, Reading, 1975; reissued by World Scientific, Singapore, 1998).
[41] B. Buck, C. B. Dover, and J. P. Vary, Phys. Rev. C **11**, 1803 (1975).
[42] B. Buck, A. C. Merchant, and S. M. Perez, Phys. Rev. C **51**, 559 (1995).
[43] T. Siiskonen, P. O. Lipas, and J. Rikovska, Phys. Rev. C **60**, 034312 (1999).
[44] R. R. Rodríguez-Guzmán, J. L. Egido, and L. M. Robledo, Eur. Phys. J. A **17**, 37 (2003).
[45] B. H. Wildenthal, Prog. Part. Nucl. Phys. **11**, 5 (1984).
[46] Y. Utsuno, T. Otsuka, T. Mizusaki, and M. Honma, Phys. Rev. C **60**, 054315 (1999).
[47] M. Belleguic *et al.*, Phys. Scr., T **88**, 122 (2000).
[48] Zs. Dombrádi *et al.*, Phys. Rev. Lett. **96**, 182501 (2006).
[49] J. R. Terry *et al.*, Phys. Lett. B **640**, 86 (2006).
[50] Y. Yanagisawa *et al.*, Phys. Lett. B **566**, 84 (2003).
[51] P. M. Endt, Nucl. Phys. A **521**, 1 (1990).
[52] H. Grawe, in *The Euroschool Lectures on Physics with Exotic Beams, Vol. I*, edited by J. Al-Khalili and E. Roeckl, Lect. Notes. Phys. **651** (Springer, Berlin Heidelberg 2004), p. 33.
[53] O. Sorlin and M.-G. Porquet, Prog. Part. Nucl. Phys. **61**, 602 (2008).
[54] A. Poves and J. Retamosa, Nucl. Phys. A **571**, 221 (1994).
[55] C. Thibault, R. Klapisch, C. Rigaud, A. M. Poskanzer, R. Prieels, L. Lessard, and W. Reisdorf, Phys. Rev. C **12**, 644 (1975).
[56] C. Détraz, M. Langevin, M. C. Goffri-Kouassi, D. Guillemaud, M. Epherre, G. Audi, C. Thibault, and F. Touchard, Nucl. Phys. A **394**, 378 (1983).
[57] T. Otsuka, Y. Utsuno, R. Fujimoto, B. A. Brown, M. Honma, and T. Mizusaki, Eur. Phys. J. A **15**, 151 (2002).
[58] A. Ozawa, T. Kobayashi, T. Suzuki, K. Yoshida, and I. Tanihata, Phys. Rev. Lett. **84**, 5493 (2000).
[59] M. Stanoiu *et al.*, Phys. Rev. C **69**, 034312 (2004).
[60] I. Angeli, Yu. P. Gangrsky, K. P. Marinova, I. N. Boboshin, S. Yu. Komarov, B. S. Ishkhanov, and V. V. Varlamov, J. Phys. G **36**, 085102 (2009).
[61] D. J. Vieira and J. M. Wouters, in *Nuclei Far from Stability, Proceedings 5th International Conference, Rosseau Lake, Ontario, Canada, 1987, Vol. 164*, edited by I. S. Towner (AIP Conference Proceedings, Melville, 1988), p. 1.
[62] Z. Dlouhý, D. Baiborodin, J. Mrázek, and G. Thiamová, Nucl. Phys. A **722**, C36 (2003).
[63] W. D. Myers and K.-H. Schmidt, Nucl. Phys. A **410**, 61 (1983).
[64] K. Kumar, Phys. Rev. Lett. **28**, 249 (1972).
[65] T. Neff and H. Feldmeier, Int. J. Mod. Phys. E **17**, 2005 (2008).
[66] G. A. Lalazissis, A. R. Farhan, and M. M. Sharma, Nucl. Phys. A **628**, 221 (1998).
[67] J.-P. Ebran, E. Khan, D. Peña Arteaga, and D. Vretenar, Phys. Rev. C **83**, 064323 (2011).
[68] L. S. Geng, H. Toki, A. Ozawa, and J. Meng, Nucl. Phys. A **730**, 80 (2004).
[69] S. Goriely, F. Tondeur, and J. M. Pearson, At. Data Nucl. Data Tables **77**, 311 (2001).
[70] H. Sagawa, X. R. Zhou, X. Z. Zhang, and T. Suzuki, Phys. Rev. C **70**, 054316 (2004).
[71] G. A. Lalazissis, D. Vretenar, and P. Ring, Eur. Phys. J. A **22**, 37 (2004).